

FLORIDA STATE UNIVERSITY
COLLEGE OF ENGINEERING

ULTRAFAST LASER MACHINING OF DIELECTRICS:
A SHARP INTERFACE MODEL

By

PETER WOERNER

A Thesis submitted to the
Department of Mechanical Engineering
in partial fulfillment of the
requirements for the degree of
Master of Science

2016

ProQuest Number: 10190743

All rights reserved

INFORMATION TO ALL USERS

The quality of this reproduction is dependent upon the quality of the copy submitted.

In the unlikely event that the author did not send a complete manuscript and there are missing pages, these will be noted. Also, if material had to be removed, a note will indicate the deletion.



ProQuest 10190743

Published by ProQuest LLC (2018). Copyright of the Dissertation is held by the Author.

All rights reserved.

This work is protected against unauthorized copying under Title 17, United States Code
Microform Edition © ProQuest LLC.

ProQuest LLC.
789 East Eisenhower Parkway
P.O. Box 1346
Ann Arbor, MI 48106 – 1346

Peter Woerner defended this thesis on July 8, 2016.
The members of the supervisory committee were:

William Oates
Professor Directing Thesis

Shangchao Lin
Committee Member

Wei Guo
Committee Member

The Graduate School has verified and approved the above-named committee members, and certifies that the thesis has been approved in accordance with university requirements.

ACKNOWLEDGMENTS

I would gratefully thank the DOE for providing funds to support this research under grant DOE-FE0012370. I would also like to thank Dr. William Oates for his incredible guidance and patience with me. I would also like to thank group members Justin Collins, Pauls Miles, Matt Worden, Sadiyah Sabah Chowdhury, Wei Gao and Harman Bal and fellow graduate student Jason Brown for numerous insightful conversations as well as numerous less insightful but entertaining conversations. I would also like to thank Dr. Wei Guo and Dr. Shangchao Lin for agreeing to be part of my committee.

PREVIEW

TABLE OF CONTENTS

List of Tables	v
List of Figures	vi
Abstract	viii
1 Background	1
1.1 Theoretical Background	1
1.2 Machining Characteristics	2
1.3 Computational Modeling	3
1.3.1 Free Electron Density Modeling of Laser Ablation in Dielectrics	3
1.3.2 Two-Temperature Model	4
1.3.3 Thermal Explosion Model	5
1.3.4 Further Work	5
1.4 Phase Transitions	5
1.4.1 Solid-Liquid Formulation	7
1.4.2 Electronic Structure Formulation	8
1.5 Uncertainty Quantification	11
1.6 Overview	13
2 Governing Equations	15
2.1 Material Kinetics	15
2.2 Electromagnetics	16
2.3 Coupling	17
2.4 Summary	20
3 Numerical Approximation and Simulation	22
3.1 Numerical Implementation	22
3.1.1 Parabolic Approximation	22
3.1.2 Beer's Approximation	23
3.1.3 Numerical Approximation of Material Kinetics	23
3.1.4 Coupling	23
3.1.5 Uncertainty Quantification Implementation	24
3.2 Energy Coupling	25
3.2.1 Standard Force Model	31
3.2.2 Coupled Force Model	34
4 Conclusions	39
Appendix	
A Computer Implementation	41
A.1 Numerical Implementation	41
Bibliography	42
Biographical Sketch	44

LIST OF TABLES

2.1	Summary of Models Tested. Parameters which are unmentioned are assumed to be deterministic. Parameters in the left column are treated as random parameters. . . .	21
3.1	The default parameter values for the energy coupling model and used in Figures 3.4, 3.7, 3.8, 3.9, and 3.10 except for parameter changes which are explicitly specified. The time step is given by the pulselength (p) times the temporal discretization constant (k) so that $\Delta t = kp$. Likewise, the spatial step is given by the $\Delta x = x_0 * h$	26
3.2	Key parameters for the standard force model.	32
3.3	Summary of mean and standard deviations from the MCMC/DRAM analysis shown in Figure 3.13. In this case the mobility is fixed at $\beta = 10^{-13} \frac{Ns}{m^3}$	34
3.4	Key parameters for the coupled force model.	37
3.5	The means and standard deviations from the MCMC/DRAM analysis shown in Figure 3.15.	37
3.6	Table comparing the different parameter values between the two constitutive models. Note that in the coupled force model, κ_1 and κ_2 are calculated using $\kappa = \beta q^2$. κ_1 was unidentifiable in the first model due to its insensitivity. β was unidentifiable in the first model, so the more relevant comparisons of $\tau = \frac{\beta}{a}$ and $\frac{\beta}{q_1}$ are included.	37

PREVIEW

LIST OF FIGURES

1.1	Visible cracks in machined sapphire. Includes blown up views to show greater details of damage. Credit Daniel Blood[6]	2
1.2	Schematic representation of probability amplitude phase-field interpretation by Meekev and Chernov[22] pulled from Boettinger et al[7]	7
1.3	This diagram shows the connection between the models. See Table 2.1 for details. . .	14
1.4	Diagram showing numerical strategy including analytic and numeric approximations .	14
3.1	Numerical approximation for verification of the linear Beer’s law visually identical to the analytic solution using 4096 data points	23
3.2	Numerical approximation for verification of our sharp interface model. This model uses initial conditions for a linear varying ρ with respect to x	24
3.3	Convergence of solutions for number of spatial points, N with $\frac{\Delta t}{\Delta x}$ fixed as $\Delta t \Delta N = 4.096 \times 10^{-12}$. The values used for this test are the mean values from the Monte Carlo sampling given in Table 3.6. The fluence used was 15.4 J/cm^2	25
3.4	Ablation depth vs. intensity for varying (a) $\beta \frac{\text{Js}}{\text{m}^3}$ (b) $\sigma_1 \frac{\text{S}}{\text{m}}$ (c) $\sigma_2 \frac{\text{S}}{\text{m}}$ and (d) $a \frac{\text{J}}{\text{m}^3}$	26
3.5	Scatter plots for (a) β (b) σ_1 (c) σ_2 and (d) a with 5000 iterations. All the parameters are random variables and therefore these plots can be seen as conditional probability realizations	28
3.6	Scatter plot of β and σ_2 with a red * representing the parameter values with ablation depth $d \in (0\text{nm}, 90\text{nm})$	29
3.7	Identification of σ_2 values that fit the data	29
3.8	Identification of β values that fit the data.	30
3.9	Model Prediction using a linear fit of β	30
3.10	DRAM fitting on β and σ_2 . Note that for σ_2 the units are given in $10^5 S/m$ and not in S/m as everywhere else in the paper.	31
3.11	DRAM fitting on β for all intensities.	32
3.12	Global scatter plots for the six material parameters with 100,000 points for the standard force model.	33
3.13	These figures show the convergence of our parameters using the DRAM algorithm[16]. In this case, the mobility is fixed at $\beta = 10^{-13} \frac{\text{Ns}}{\text{m}^3}$. (a) The chains include the last 50,000 iterations. (b) Posterior densities of the model parameters. (c) Pair correlations between each set of parameters. (d) Model prediction including 95% prediction intervals (PI) and 95% credible intervals (CI).	35

3.14	Local sensitivities of key material parameters about the the mean values given in Table 3.3 for the standard force model. The parameter varied in these simulations is given in the legend with all other values held fixed at their mean values. The units are as follows: q ($\frac{C}{m^3}$), κ_2 ($\frac{1}{m}$), β ($\frac{Ns}{m^3}$), a ($\frac{N}{m^3}$)	36
3.15	These figures show the convergence of our parameters using the DRAM algorithm [16]. (a) The chains show the last 100,000 iterations. (b) Posterior densities of the model parameters is plotted. (c) Pair correlations between all model parameters is based on the 100,000 samples. (d) Model prediction including the 95% prediction and credible intervals. Note that a is scaled by factor of 10^{15} . The units are as follows: q_1 ($\frac{C}{m^3}$), q_2 ($\frac{C}{m^3}$), β ($\frac{Ns}{m^3}$), a ($\frac{N}{m^3}$).	38

PREVIEW

ABSTRACT

High temperature pressure sensing is desirable for a broad range of applications related to re-entry of space vehicles and control of combustion processes; however, limited materials can sustain temperatures above 1000°C while under time-varying pressure. A sapphire based optical pressure transducer has been proposed for measuring pressure at temperatures approaching 1600°C . Manufacturing such sensors has focused on picosecond laser machining. Current research has produced models which can predict material ablation for longer (ns) pulses and shorter (fs) pulses but there is an underwhelming amount of research focusing on predicting and understanding the mechanics of picosecond pulses. This is partially because of transitions in the mode of ablation processes associated with photothermal versus photochemical behavior. We put forth a general model for laser ablation using Maxwell's equations and a sharp interface equation and compare different constitutive laws which couple the two equations together. The proposed modeling results are compared to laser machining experimental data on sapphire from the literature to illustrate key material parameter uncertainty and sensitivity to the laser machining process. Bayesian uncertainty quantification is used to help validate the approximations within the constitutive equations.

CHAPTER 1

BACKGROUND

1.1 Theoretical Background

High powered laser-sapphire interactions have long been of interest to those studying fundamental physics. This research has found numerous engineering applications including microfluidics, microsensors, optical windows, abrasion resistant mechanical contacts, buffer materials and high power laser construction. Therefore, numerous computational and experimental studies have been performed regarding milli-, micro-, nano-, pico- and femtosecond laser ablation. The first step of light-matter interaction is non-thermal absorption (electron excitation) through either multiphoton ionization, defect allowed single-photon ionization or inverse Bremsstrahlung[9] [26]. Only multiphoton ionization is allowed in pristine equilibrium sapphire on the basis of sapphire's large bandgap energy of $\approx 8.8\text{eV}$ [17]. Absorption is followed by complex material processes. In general this secondary process is classified as either photothermal (pyrolytic), photochemical (photolytic) or photophysical (both thermal and chemical). This classification is difficult because it can depend on many different parameters including laser pulse duration, fluence, material properties and material defects[18]. Conventionally, pulse length is considered the leading determinant of classification. However, experimental measurements have shown that sapphire is unconventional. Millisecond pulses have been quantified to produce thermal melting[17]. Nanosecond pulse measurements are believed to generate electron sputtering[3], a photochemical process. This is concluded from temperature measurements of the ablation plume[12][13]. Faster pico- and femtosecond pulsed laser-sapphire interactions have proven to be more complex.

The complexity of pico- and femtosecond pulsed laser interaction is strongly dependent on material defects. Defects play a large role in laser induced damage of dielectrics[21]. Nowhere can this be seen more clearly than in sapphire's two ablation phases: the gentle phase and the strong phase[3]. Experimental results have suggested that the transition from the gentle to strong phase is due to the number of defects and inclusions in the material[3]. The gentle phase is characterized by a lower rate of removal and a polishing surface effect while the strong phase has a significantly larger rate of removal and tends to have a rough surface finish [4]. Although separate gentle and strong phases do not generally exist in other dielectrics[2], these materials still see huge

variability in ablation depth and threshold due to defects[21]. The gentle phase is considered to be a photochemical effect: either Coulomb explosion or particle vaporization. The strong phase is considered to be a photothermal effect, specifically phase explosion[4][20]. This separation into gentle and strong phases works well when $\tau_{pulse} \lesssim 4\text{ps}$, however the physical characteristics begin to blend together when $\tau_{pulse} \gtrsim 4\text{ps}$ [4]. This leaves classification of picosecond lasers an open question.

1.2 Machining Characteristics

Collaborators at the University of Florida have pursued three desirable types of cuts for laser processing of sapphire: through, face and pocket[6]. Through-milling produces a cut through the entire material with a desired profile. Face-milling is used to reduce the thickness of a workpiece. Pocket-milling is used to produce a given depth feature[6]. These different cuts can have an effect on the processing strategy and laser parameters. Therefore, it is imperative to properly model the physics and material response for different laser parameters.

The modeling research presented here is primarily meant to provide a fundamental approach to predicting picosecond laser ablation. A key question pertains to excessive pulsing that produces undesirable material removal and machining defects. Excessive pulsing can occur due to starting/stopping, small radius turns and command delays. As seen in Figure 1.1, excessive pulsing in H-bar test cuts at the University of Florida have produced undesirable microcracks[6].

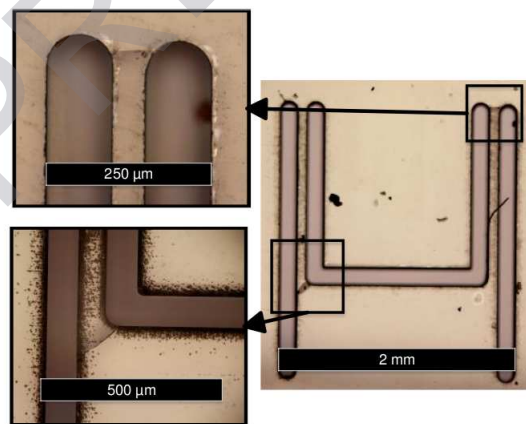


Figure 1.1: Visible cracks in machined sapphire. Includes blown up views to show greater details of damage. Credit Daniel Blood[6]

There are also other mechanics of material issues to address. Nanoscale indentation on laser machined specimens have an unexplained toughening of the material on the laser ablation surface.